https://dx.doi.org/10.1016/j.jmps.2021.104642

Tension-compression asymmetry of the stress-strain behavior of the stacked graphene assembly: Experimental measurement and theoretical interpretation

Yang Gao,[a,b,c†] Yujie Xie,[a,b,†] Anran Wei,[b] Yujie Wei,[c,d] Tao Chen,[e,f] Haimin Yao[a,b,*]

[a]The Hong Kong Polytechnic University Shenzhen Research Institute, Shenzhen, Guangdong 518057, China
[b]Department of Mechanical Engineering, The Hong Kong Polytechnic University, Kowloon, Hung Hom, Hong Kong SAR, China
[c]State Key Laboratory of Nonlinear Mechanics (LNM), Institute of Mechanics, Chinese Academy of Sciences, Beijing 100190, China
[d]School of Engineering Sciences, University of Chinese Academy of Sciences, Beijing 100049, China
[e]Key Laboratory of Marine Materials and Related Technologies, Zhejiang Key Laboratory of Marine Materials and Protective Technologies, Ningbo Institute of Materials Technology and Engineering, Chinese Academy of Sciences, Ningbo 315201, China
[f]School of Chemical Sciences, University of Chinese Academy of Sciences, Beijing 100049, China

[*]To whom correspondence should be addressed: mmhyao@polyu.edu.hk

[†]These authors contributed equally.

Abstract: Two-dimensional (2D) materials as exemplified by graphene have received a bunch of attention for their outstanding properties and enormous application potential. Recently, a macroscopic graphene-based material was fabricated simply by stacking the few-layer graphene flakes. The resulting film, called SGA, exhibits unusual mechanical behavior, which implies the existence of tension-compression asymmetry in its mechanical property. However, direct experimental verification of such unique mechanical property of the SGA remains deficient because of the difficulty in fixturing and applying load on the samples. In this work, we tackle these problems by transferring the SGA film onto a polyethylene (PE) substrate which can elongate and contract in response to the variation of the ambient temperature. Tensile and compressive loads thus can be controllably applied to the SGA samples through the SGA/PE interface by tuning the temperature variation. The stress-strain curves of the SGA, including tensile and compressive, are deduced based on the Stoney equation for thin film-substrate systems, showing the tension-compression asymmetry as expected. Theoretical modeling is carried out and reveals the structural basis

of such unique mechanical behavior. This work not only provides a facile yet effective approach to measuring the stress-strain behavior of less-cohesive materials like SGA but also is of great value to the design and applications of SGA and other stacked assemblies of 2D materials in flexible sensors and actuators.

Keywords: Two-dimensional materials; Thin film; Stoney equation; Stacked assembly; Less-cohesive materials

1. Introduction

Two-dimensional (2D) materials refer to crystalline materials consisting of one or a few layers of atoms along the thickness direction. Recent years have witnessed the surging research interest in 2D materials and breakthroughs in this field. So far, a large family of 2D materials has been reported, including graphene, h-BN, 2D oxides, transition metal chalcogenides, 2D van der Waals heterostructures, β-Silicene, black phosphorus nanosheets, etc. Due to the ultrathin thickness and ultrahigh specific surface area, 2D materials exhibit a range of fascinating electronic, optical, and mechanical properties that are normally absent in their bulk counterparts (Bhimanapati et al., 2015; Geim, 2009; Nakada et al., 1996; Sorkin et al., 2017), implying great potentials in diverse applications including flexible electronics (Fiori et al., 2014; Kim et al., 2015), nanocomposites (Kim et al., 2010; Potts et al., 2011), photodetectors (Huo and Konstantatos, 2018; Long et al., 2019), energy storage devices (Pomerantseva and Gogotsi, 2017; Zhang et al., 2016), etc. To acquire high-quality 2D materials, a variety of physical and chemical methods have been developed, including mechanical exfoliation (Huang et al., 2015; Novoselov et al., 2004), liquid exfoliation (Coleman et al., 2011; Hanlon et al., 2015), thermal reduction (Chen et al., 2010) and chemical vapor deposition (Gupta et al., 2015; Jeon et al., 2015). However, the fabrication process of large-area high-quality 2D materials is generally complicated and involves costly equipment for achieving the required ultravacuum and high-temperature conditions. In contrast, small-area few-layer 2D materials, such as few-layer graphene flakes, can be produced by liquid exfoliation in large quantities at a low cost. One of the promising applications of such small-area flakes is to assemble them into macroscopic thin films via techniques such as vacuum filtration method (Hernandez et al., 2008) and Langmuir-Blodgett (L-B) method (He et al., 2019). Although the assembled

graphene flakes cohere with each other through the weak van der Waals forces, excellent electrical conductivity was observed in the SGA film, making it an excellent candidate for soft conductive materials in sensors (He et al., 2019; Li and Yang, 2020). In addition, the mechanical behavior of the SGA film was also found unique. In our earlier study, the SGA was found to exhibit asymmetric elastoplasticity under tension and compression. Specifically, it exhibits apparent plasticity under tension while pure elasticity under compression, which endows the SGA-based soft actuators with great configurational programmability (Wang et al., 2020). However, this property of the SGA was inferred from the thermal-induced curling behavior of the SGA-based bilayer films and was testified merely by molecular dynamics (MD) simulation. The direct measurement of the mechanical behaviors of SGA under tension and compression remains deficient, not to mention the revelation of the underlying structure-property relations. The technical difficulty of experimentation mainly lies in the less-cohesive and fragile nature of the SGA films, which can be hardly clamped using the traditional fixturing method. Another challenge is the possible buckling of the freestanding SGA film under compression, which deters the possibility to measure the property of SGA under compression with the traditional testing method. To tackle these problems, in this paper, we transfer the SGA film on a polyethylene (PE) substrate, a thermal-responsive film, to form a thin film/substrate bilayer system. By increasing or decreasing the ambient temperature, the PE substrate tends to extend or contract while the SGA is relatively inert to the temperature variation, resulting in the tensile or compressive load applied on the SGA film through the interface with the PE substrate. By using the Stoney relation for thin film and substrate system, the stress and strain of the SGA can be deduced from the measured bending curvature of the bilayer structure, giving rise to the stress-strain curves under tensile and compressive loadings. To gain an insightful understanding of the experimental results, theoretical modelling is carried out to explore the structural dependences of the characteristic mechanical properties of the SGA including the elastic moduli under tension and compression as well as the tensile strength. The whole paper is concluded by discussing the potential applications of the results and the limitation of the present work.

2. Experimental measurement

2.1 Theoretical basis of the testing approach

Due to the weak cohesion between graphene flakes as well as the small thickness of SGA film, preparing a free-standing SGA sample remains challenging, not to mention fixturing and applying loads on it. To tackle these problems, we constructed a bilayer structure by transferring an SGA film on a PE substrate which can expand or contract in response to the variation of temperature (ΔT). As the thermal expansion of graphene is negligibly low, the strain misfit between the SGA film and PE substrate will lead to internal thermal stress and bending of the SGA/PE bilayer. Since the van der Waals interaction between PE and graphene is stronger than that between graphene flakes in SGA film (Pang et al., 2019), we assume that the SGA film keeps attached on the PE substrate when deforming upon loading. The bending curvature (κ) depends on the temperature change and the dimensions and mechanical properties of the SGA film and PE substrate (see Fig. 1(a)). The well-known Stoney equation correlates the film stress in the SGA with the bending curvature (κ) of the bilayer as (Freund and Suresh, 2004)

$$\sigma_{\mathrm{SGA}} = \frac{E^*_{\mathrm{PE}} t^2_{\mathrm{PE}} \kappa}{6 t_{\mathrm{SGA}}} \tag{1}$$

where $E^*_{\mathrm{PE}} \equiv \frac{E_{\mathrm{PE}}}{1-\nu^2_{\mathrm{PE}}}$ is the plane strain modulus of the PE layer with E_{PE} and ν_{PE} being the Young's modulus and Poisson's ratio, and t_{SGA} and t_{PE} are the thicknesses of the SGA film and PE substrate respectively. The validity of Eq. (1) requires $t_{\mathrm{SGA}} \ll t_{\mathrm{PE}}$. This condition is satisfied in our SGA/PE bilayers. It should be pointed out that Eq. (1) is based on the plane strain, rather than biaxial, assumption for the stress state of the bilayer. This is because the thermal expansion of the PE film is much higher along the direction with preferred molecular alignment, which was selected as the longitudinal direction of the film during our sample preparation. Therefore, the bending of our SGA/PE bilayers mainly happens about the transverse axis, as schematically shown in Fig. 1(a).

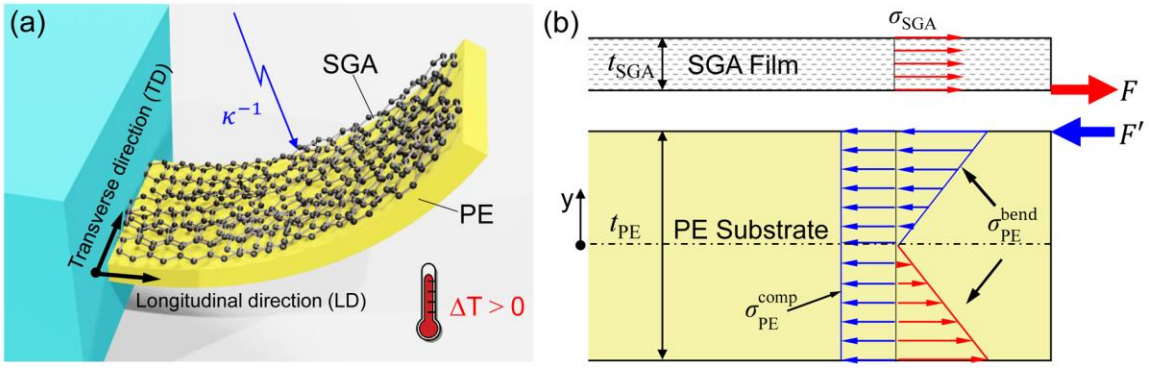

Fig. 1. Schematic illustrations showing (a) the setup for the measurement, (b) force and stress experienced by the SGA film and PE substrate.

For the PE substrate, which is subjected to an eccentric axial compressive force $F' = t_{SGA}\sigma_{SGA}$ near the top surface (Fig. 1(b)), the strain near its top surface is given by

$$\varepsilon_{PE}^{top} = (\alpha_{LD} + \alpha_{TD}\nu_{PE})\Delta T - \frac{4t_{SGA}}{E_{PE}^{*}t_{PE}}\sigma_{SGA} \quad (2)$$

where α_{LD} and α_{TD} are the coefficients of thermal expansion of the PE substrate along the longitudinal and transverse direction, respectively, and ΔT is the variation of temperature from the ambient temperature. ΔT could be positive or negative. In Eq. (2), the first term stands for the thermal strain along the longitudinal direction with transverse strain constrained and the second term represents the elastic strain caused by the eccentric axial compression. Continuity of strain across the SGA/PE interface requires that the strain in the SGA (ε_{SGA}) should be equal to ε_{PE}^{top}, which upon the substitution of Eq. (1) gives rise to

$$\varepsilon_{SGA} = \varepsilon_{PE}^{top} = (\alpha_{LD} + \alpha_{TD}\nu_{PE})\Delta T - \frac{2t_{PE}\kappa}{3} \quad (3)$$

For a given ΔT, the bending curvature κ in Eqs. (1) and (3) can be measured experimentally (see Section 2.3). Therefore, the stress and strain of the SGA layer can be deduced according to Eqs. (1) and (3) respectively if the values of E_{PE}, ν_{PE}, α_{LD} , α_{TD}, t_{SGA}, t_{PE} are known. Preliminary measurements indicated that $\alpha_{LD} = 3.58 \times 10^{-4}\ ^{\circ}C^{-1}$ and $\alpha_{TD} = 2.54 \times 10^{-4}\ ^{\circ}C^{-1}$ (see Appendix A), $\nu_{PE} = 0.46$ (Ladizesky and Ward, 1971), $t_{PE} = 10\ \mu m$. The elastic modulus of the PE layer exhibits strong temperature dependence, which can be expressed as $E_{PE}(T) = 0.045T^2 - 6.53T + 284.6$ (see Appendix B), with T

being the temperature ranging from −20℃ to 60℃. Due to the stacking structure of the SGA and the rough surface, the measurement of the thickness of the SGA film (t_{SGA}) is not straightforward and deserves an elaboration as below.

2.2 Measurement of the thickness of the SGA films

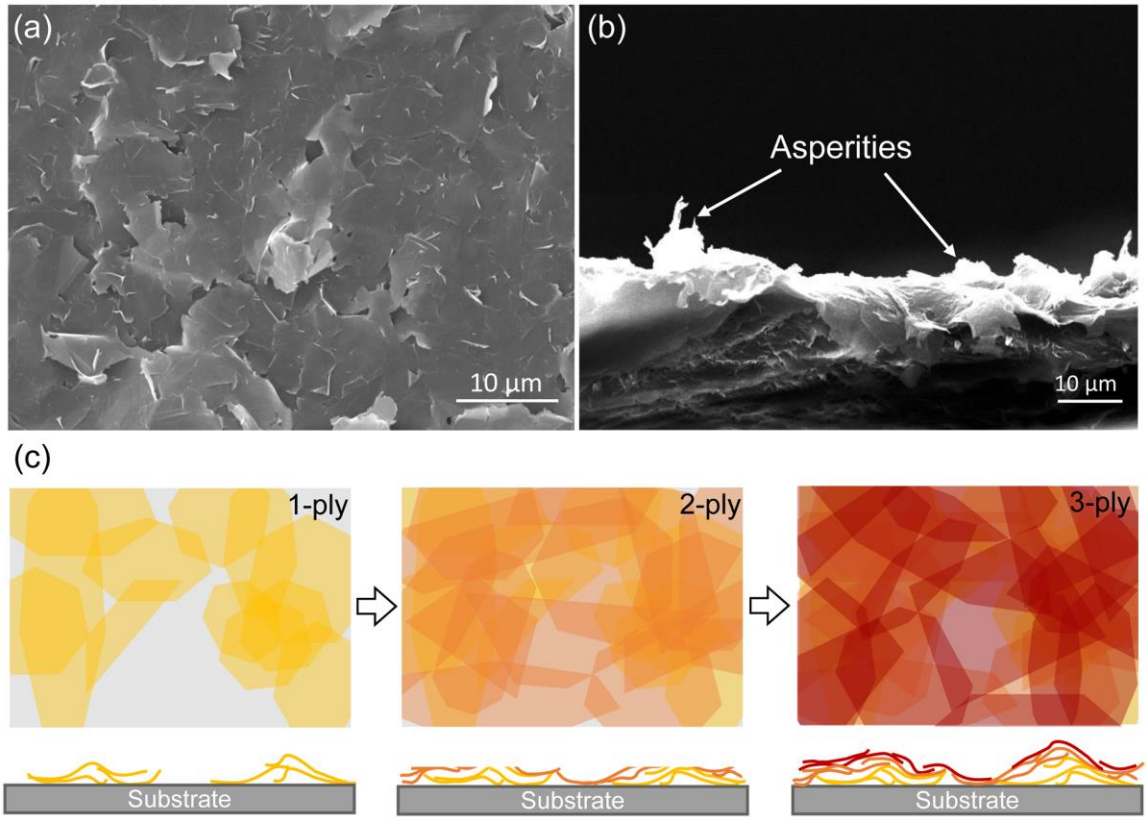

Fig. 2. SEM images of (a) top view and (b) cross-section of the prepared SGA film. (c) Schematic diagram showing the structure of SGA film as ply number increases.

Our SGA samples were produced by following the L-B method reported in the literature (Wang et al., 2020). The top and cross-sectional SEM images of SGA film show that the staggered graphene flakes form a stacked structure (see Fig. 2(a, b)). Thicker SGA film can be obtained by repeating the transferring process in the L-B method multiple times. One more time of transferring gives rise to an additional ply of flakes, as schematically shown in Fig. 2(c). The thicknesses of the SGA films with different ply numbers were measured by a stylus surface profiler (DektakXT, Bruker). Given the small size of graphene flakes (5-10 μm in-plane dimension), a combination of low scanning speed (50 μm/s, the lower limit of the apparatus) and high sampling rate (0.167 μm/point) was employed to

ensure a precise capture of the profile features of the SGA film. Fig. 3(a) shows the typical profiles of the 1-ply and 6-ply SGA films. It can be seen that the height profiles exhibit abrupt peaks resulting from the asperities on the SGA surface (see Fig. 2(b)). If the mean value of the profile height at all the sampling points (the blue dashed line in Fig. 3(a)) is taken as the thickness of the SGA, apparently an overestimated thickness will be obtained. To eliminate the noise brought by the surface asperities, we calculated the probability density of the thickness at the sampling points, as displayed in Fig. 3(a). The height with density peak (the red dashed line) represents the height that is most frequently examined during scanning, namely the mode of the measurements. It describes the thickness of the SGA film better than the mean height does. Therefore, the height with peak probability density, instead of the mean value, is taken as the SGA film thickness (t_{SGA}) in our studies below. Fig. 3(b) shows the measured t_{SGA} for SGA films with different ply numbers. These values will be used later when determining the stress and strain in the SGA film.

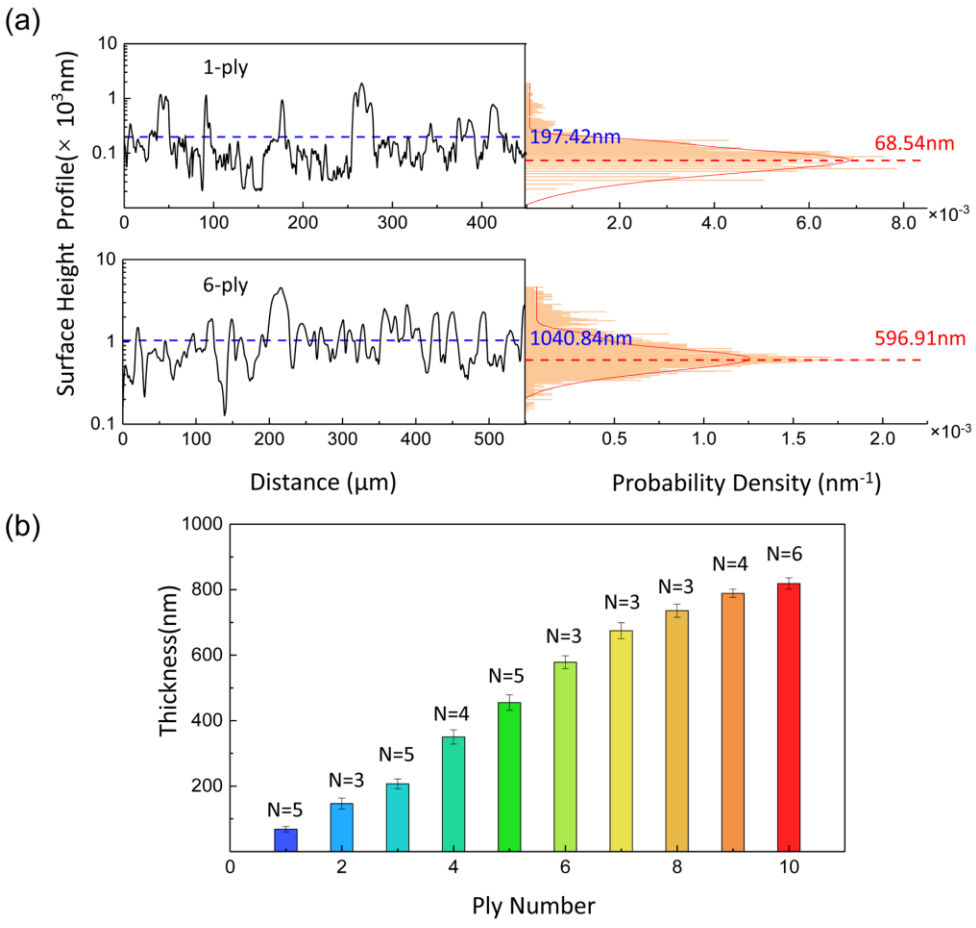

Fig. 3. (a) Representative surface height profiles of 1-ply and 6-ply SGA films and their corresponding probability densities. (b) Measured thicknesses of SGA films with different ply numbers from 1 to 10. Here, *N* stands for the number of the tested samples.

2.3 Measurement of the bending curvature

The curvature measurement of SGA/PE bilayer was performed in a homemade temperature test chamber. The SGA/PE bilayer samples were clamped at one end and the other end was free. A thermocouple was placed nearby to monitor the temperature in real-time. For loading, the temperature in the chamber was increased or decreased at a rate of 0.5℃/min from the room temperature (~25℃). In our experiments, the temperature varied in the range of 25~60 ℃ for heating and −15~25℃ for cooling. For unloading, the temperature in the chamber returned to the room temperature at a rate of 0.5℃/min. In the loading and unloading processes, a digital photo was taken from the side every 2℃ change in temperature to capture the bending deflection $z(x)$, based on which the bending curvature (κ) can be deduced via $\kappa = \frac{z''}{(1+z'^2)^{3/2}}$.

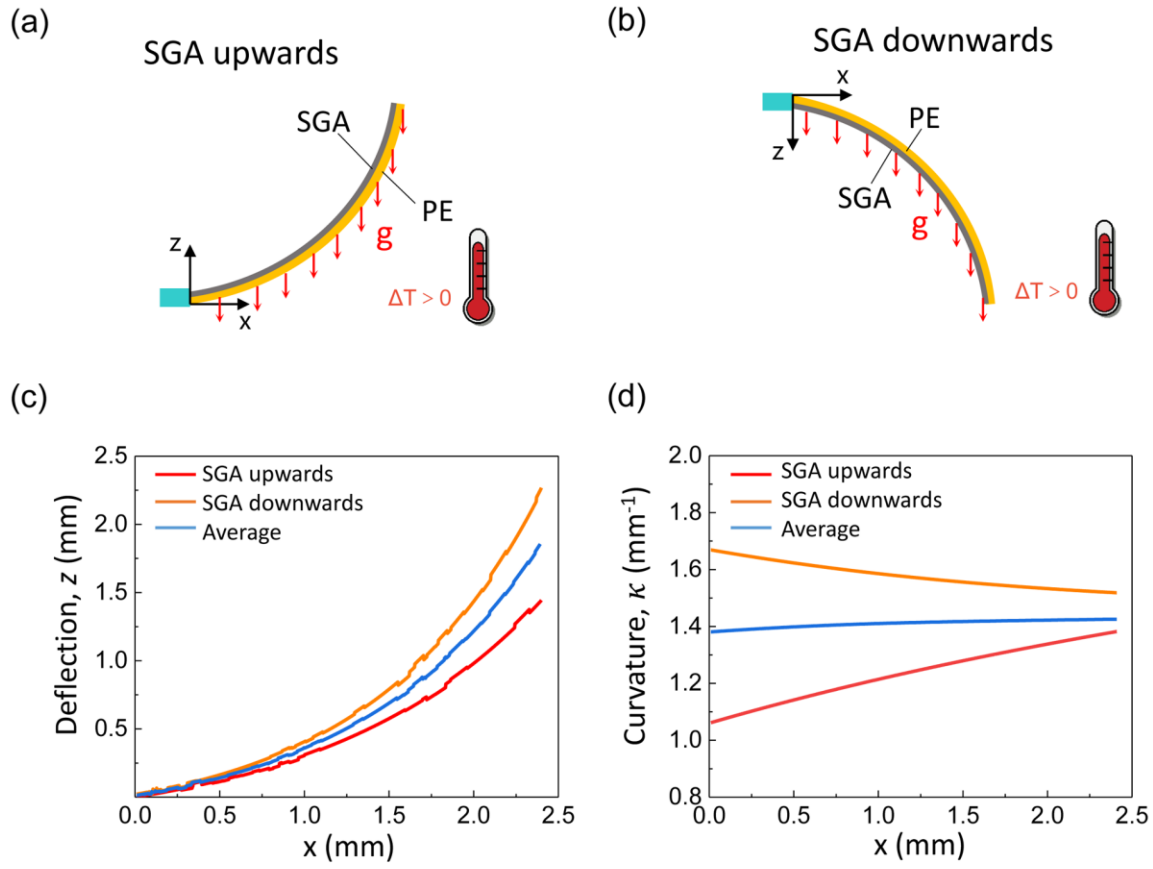

Fig. 4. Effect of gravity on the bending curvature of the SGA/PE bilayer in response to temperature variation. Schematic diagrams showing two different experimental configurations with the SGA layer (a) facing upwards and (b) facing downwards. (c) Measured deflections of the SGA/PE bilayer in two different configurations and their average; (d) Bending curvature of the bilayer calculated from the deflections in (c) through $\kappa = \frac{z''}{(1+z'^2)^{3/2}}$.

To eliminate the effect of gravity on the bending curvature, each test was conducted twice in two different testing configurations: one with the SGA layer facing upwards (see Fig. 4(a)) and the other with the SGA layer facing downwards (see Fig. 4(b)). As an example, Fig. 4(c) shows the measured deflections of a 3-ply SGA/PE bilayer in two configurations when $\Delta T = 32$ ℃ as well as their mean. The bending curvatures calculated from them are shown in Fig. 4(d). As expected, the curvature κ deduced from the mean deflection exhibits little variation with x, implying that the gravity effect has been eliminated successfully.

2.4 Measurement results: Stress-strain curves of SGA

Based on the measured curvature (κ) in combination with the other dimensional parameters and materials constants (E_{PE}, ν_{PE}, α_{LD} , α_{TD}, t_{SGA}, t_{PE}), the stress and strain of the SGA at different temperatures can be deduced. Fig. 5 (a) shows the stress-strain curves of SGA films with different ply numbers. Under tensile loading, the stress increases linearly with the strain. The slope, which represents the elastic modulus, depends on the ply number of the sample. The more the ply number, the higher the modulus (see Fig. 5(c)). Such thickness dependence of the tensile modulus might be attributed to the increased fraction of the graphene flakes with better alignment and flatness as the ply number increases. When the tensile strain reaches a critical value around 0.7%, the load-carrying capacity of the SGA films saturates, as shown by the plateaus on the stress-strain curves. Under this circumstance, unrecoverable deformation, or plastic deformation, happens in the SGA films upon further loading. This can be confirmed by a follow-up unloading process as shown in Fig. 5(b). On the other hand, under compressive load, the stress increases linearly with the strain, indicating a pure elastic deformation. Such elasticity can be fully recovered upon unloading, as shown in Fig. 5(b). Similarly, the slope of the curve,

which represents the compressive modulus, increases with the ply number (see Fig. 5(c)). The obtained asymmetric elastoplasticity of the SGA film, namely, elastic-perfectly plastic under tension while purely elastic under compression, affirms our previous inference indeed (Wang et al., 2020).

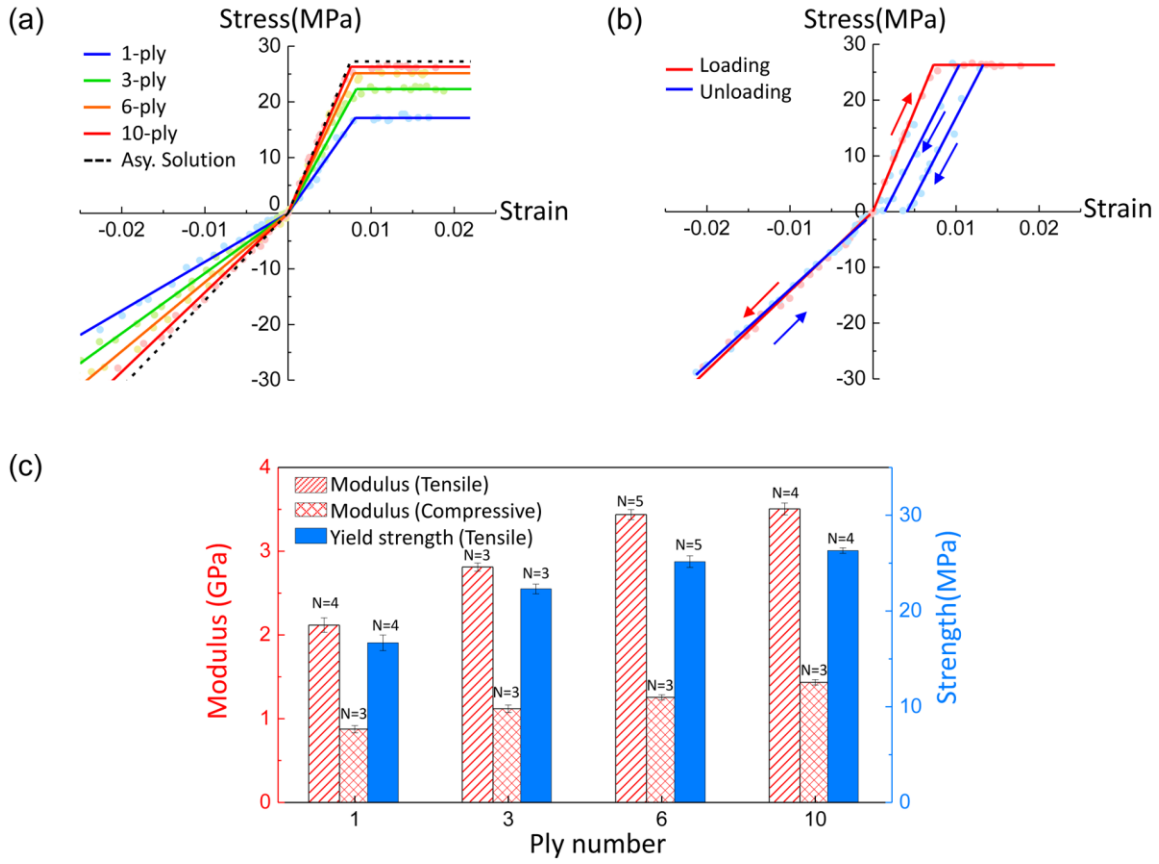

Fig. 5. (a) Measured stress-strain curves of SGA film of different plies. Here, the solid lines represent the fitting curves of the experimental results, while the dashed ones represent the theoretical predictions. Model parameters adopted in the prediction of tensile curves: $E_{\mathrm{GF}} = 4$ GPa, $G_{\mathrm{in}} = 400$ MPa, $\tau_{\mathrm{in}} = 30$ MPa, $h_{\mathrm{GF}} = 10$ nm, $l = 5$ μm, $h_{\mathrm{in}} = 1$ nm. Model parameters adopted in the prediction of compressive curves: $E_{11} = 3.5$ GPa, $G_{13} = 0.7$ GPa, $E_{33} = 100$ MPa, $\nu_{12} = \nu_{13} = 0.1$. (b) The measured loading-unloading stress-strain curves for the SGA films with 10 plies. (c) The dependence of the mechanical properties of SGA films (tensile modulus, compressive modulus, and yield strength under tension) on the ply number. Here, *N* stands for the number of the tested samples.

3. Theoretical interpretation of the measured results

The experimental measurements above reconfirm the asymmetric elastoplastic behavior of the SGA film, which can be fully depicted by three characteristic parameters:

tensile modulus ($E_{\mathrm{SGA}}^{\mathrm{t}}$), tensile strength ($S_{\mathrm{SGA}}^{\mathrm{t}}$), and compressive modulus ($E_{\mathrm{SGA}}^{\mathrm{c}}$). To disclose the dependence of these parameters on the microscopic structure of the SGA and the mechanical properties of the building graphene flakes, theoretical modeling was carried out.

3.1 Tensile properties of SGA

By neglecting the non-uniformity of the graphene flakes in dimension and shape as well as the possible imperfect alignment of them, we model the SGA film as a staggered multilayer structure of identical flakes with length $2l$ and thickness h_{GF}, as shown in Fig. 6(a). Since the interactions between the adjacent graphene flakes in SGA originate from the van der Waals interaction which is shearing dominant when the SGA film is subject to remote tensile load (Yao et al., 2013), an artificial continuum layer then is introduced between the adjacent graphene flakes to model the interaction between them. Here, the graphene flakes are modeled as a purely elastic material with Young's modulus and Poisson's ratio being E_{GF} and ν_{GF}, while the artificial interface layer is assumed elastic within the interaction range with shear modulus and shear strength being G_{in} and τ_{in}, respectively (see Fig. 6(b)). The periodicity and symmetry of the model allow us to consider a representative volume element (RVE) as shown in Fig. 6(c).

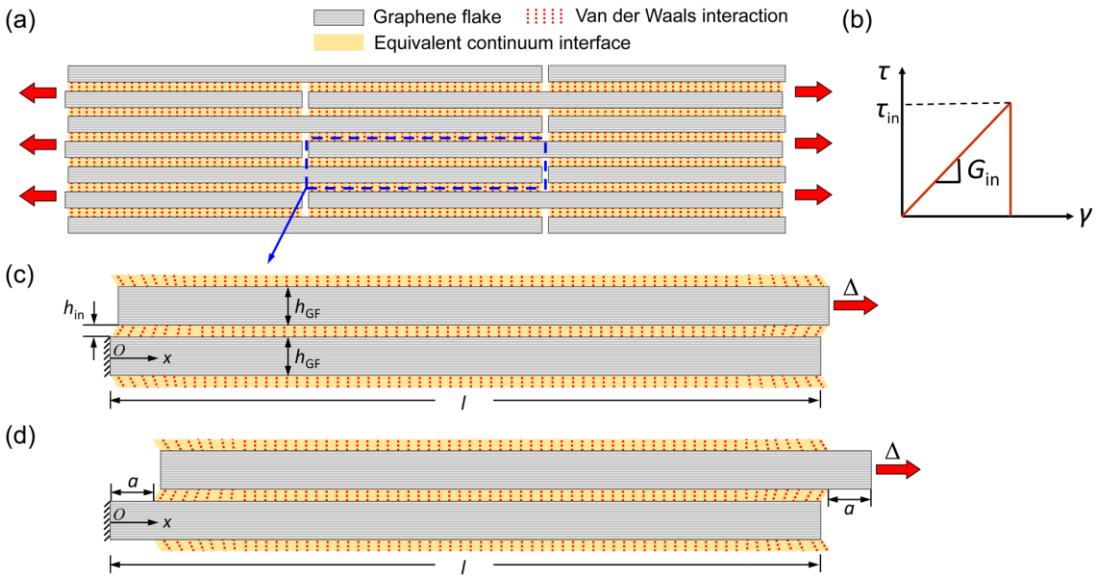

Fig. 6. (a) Staggered multilayer structure of the SGA. (b) The constitutive relation adopted to describe the intermolecular interaction between the graphene flakes. Illustrations of (c) the representative volume element (RVE) adopted to model the tensile behavior of SGA,

and (d) the configuration of the RVE at the stage II of deformation in which the sliding between graphene flakes in the SGA happens under excessive tension.

Upon an ever-increasing displacement load Δ, the mechanical response of the RVE model will experience two stages. At stage I (see Fig. 6(c)), when the displacement load Δ remains small, the whole RVE including the interface layer undergoes purely elastic deformation only, and the shear stress distribution along the interface is given by (Yao et al., 2013)

$$\tau(x) = \frac{G_{\text{in}}\Delta}{h_{\text{in}}} \cdot \frac{\cosh(2\mu x/l-\mu)}{\cosh\mu+\mu\cdot\sinh\mu} \, (0 \le x \le l) \tag{4}$$

where dimensionless parameter $\mu \equiv \sqrt{\frac{l^2 G_{\text{in}}}{h_{\text{GF}} h_{\text{in}} E^*_{\text{GF}}}}$ with $E^*_{\text{GF}} \equiv \frac{E_{\text{GF}}}{1-\nu^2_{\text{GF}}}$ representing the plane strain modulus of graphene flake, h_{GF} and h_{in} representing the thickness of an individual few-layer graphene flake and artificial interface layer, respectively. Force equilibrium of graphene flakes implies that the tensile force applied on the end of RVE should be equal to the resultant force of the shear stress applied on both sides. That is,

$$F_{|x=l} = 2\int_0^l \tau(x)\mathrm{d}x = \frac{2G_{\text{in}}\Delta}{h_{\text{in}}\mu} \cdot \frac{l\cdot\tanh\mu}{1+\mu\cdot\tanh\mu} \tag{5}$$

The nominal tensile stress applied on the RVE is given by

$$\sigma = \frac{F_{|x=l}}{2(h_{\text{in}}+h_{\text{GF}})} = \frac{G_{\text{in}}\Delta}{(h_{\text{in}}+h_{\text{GF}})h_{\text{in}}\mu} \cdot \frac{l\cdot\tanh\mu}{1+\mu\cdot\tanh\mu} \tag{6}$$

Dividing the nominal tensile strain $\varepsilon \equiv \Delta/l$ on both sides of Eq. (6) gives rise to the effective tensile modulus of the SGA as

$$E^{\text{t}}_{\text{SGA}} \equiv \frac{\sigma}{\varepsilon} = \frac{G_{\text{in}}}{(h_{\text{in}}+h_{\text{GF}})h_{\text{in}}\mu} \cdot \frac{l^2\cdot\tanh\mu}{1+\mu\cdot\tanh\mu} \tag{7}$$

Similar prediction has also been made for the effective modulus of the brick-and-mortar structured biological materials (Gao et al., 2003; Liu et al., 2011a).

Since the shear stress along the interface is limited by τ_{in}, Eq. (4) implies a critical displacement load

$$\Delta_{\text{c}} = \frac{\tau_{\text{in}} h_{\text{in}}}{G_{\text{in}}} \cdot (1 + \mu \cdot \tanh\mu), \tag{8}$$

above which graphene flakes would slide with respect to each other, leading to the onset of stage II. Substituting Eq. (8) into Eq. (6) gives the yield strength of SGA as

$$S_{\mathrm{SGA}}^{\mathrm{t}} = \frac{\tau_{\mathrm{in}} l \cdot \tanh\mu}{(h_{\mathrm{in}}+h_{\mathrm{GF}})\mu} \tag{9}$$

The deformation of the RVE at stage II can be deemed as the superposition of the inter-flake sliding plus the elastic deformation under external loading (Fig. 6(d)). Then the effective stress in the RVE can be obtained simply by replacing l and Δ in Eq. (6) with $l - a$ and Δ_{c} respectively:

$$\sigma = \frac{\tau_{\mathrm{in}}\sqrt{h_{\mathrm{GF}} h_{\mathrm{in}} E_{\mathrm{GF}}^{*}/G_{\mathrm{in}}}}{h_{\mathrm{in}}+h_{\mathrm{GF}}} \cdot \tanh\left[\sqrt{\frac{(l-a)^2 G_{\mathrm{in}}}{h_{\mathrm{GF}} h_{\mathrm{in}} E_{\mathrm{GF}}^{*}}}\right] \tag{10}$$

where a stands for the sliding distance between the adjacent flakes as shown in Fig. 6(d). Here, the in-plane deformation of the sliding part (a) of the graphene flake is neglected due to its high stiffness and resultant low strain level. Even though Eq. (10) implies the dependence of σ on a, the behavior of the hyperbolic tangent function in Eq. (10) determines that such dependence is quite weak especially when $\frac{(l-a)^2 G_{\mathrm{in}}}{h_{\mathrm{GF}} h_{\mathrm{in}} E_{\mathrm{GF}}^{*}} \gg 1$. By taking typical values $E_{\mathrm{GF}} = 4$ GPa (Li et al., 2019), $\nu_{\mathrm{GF}} = 0.1$(Wei and Yang, 2019), $G_{\mathrm{in}} = 400$ MPa (Soule and Nezbeda, 1968), $\tau_{\mathrm{in}} = 30$ MPa, $h_{\mathrm{GF}} = 10$ nm, $l = 5$ μm, $h_{\mathrm{in}} = 1$ nm, it can be estimated that the hyperbolic tangent function in Eq. (10) is close to unity as a varies from 0 to $0.9l$. Therefore, the effective stress (σ) is maintained at a constant value close to $S_{\mathrm{SGA}}^{\mathrm{t}}$ in a wide range of strain which includes the unrecoverable component ($\varepsilon_{\mathrm{p}} = a/l$) due to sliding and the elastic component ($\varepsilon_{\mathrm{e}} = \Delta_{\mathrm{c}}/l$). Such stress plateau in the stage II in combination with the elastic behavior at the stage I comprise the elastic-perfectly plastic behavior of the SGA, which is consistent with our experiments above. However, since the theoretical model above did not consider the limited thickness of the SGA film along the stacking direction, the theoretical tensile modulus (E_{SGA}^{t}) and yield strength ($S_{\mathrm{SGA}}^{\mathrm{t}}$) we obtained can be deemed as their asymptotic solutions for SGA sufficiently thick, as plotted by the broken line in Fig. 5(a) based on the representative parameters mentioned above.

It can be demonstrated that the tensile modulus and yield strength of the SGA can be further simplified to be

$$E_{\mathrm{SGA}}^{\mathrm{t}} \cong \frac{E_{\mathrm{GF}}^{*} h_{\mathrm{GF}}}{h_{\mathrm{in}}+h_{\mathrm{GF}}} \tag{11}$$

$$S_{\mathrm{SGA}}^{\mathrm{t}} \cong \frac{\tau_{\mathrm{in}}}{h_{\mathrm{in}}+h_{\mathrm{GF}}} \sqrt{\frac{h_{\mathrm{GF}} h_{\mathrm{in}} E_{\mathrm{GF}}^{*}}{G_{\mathrm{in}}}} \tag{12}$$

when the non-dimensional parameter $\mu \equiv \sqrt{\frac{l^2 G_{\mathrm{in}}}{h_{\mathrm{GF}} h_{\mathrm{in}} E_{\mathrm{GF}}^{*}}} \gg 1$, implying the independence of the tensile properties on the flake length (l) then. For typical values of $E_{\mathrm{GF}} = 4$ GPa, $\nu_{\mathrm{GF}} = 0.1$, $G_{\mathrm{in}} = 400$ MPa, $h_{\mathrm{in}} = 1$ nm, this condition can be readily satisfied if the thickness and lateral size of the graphene flakes fall in the ranges of $h_{\mathrm{GF}} = 1\sim50$ nm and $l = 1\sim50$ μm, respectively. Taking typical values of $E_{\mathrm{GF}} = 4$ GPa, $\nu_{\mathrm{GF}} = 0.1$, $G_{\mathrm{in}} = 400$ MPa, $\tau_{\mathrm{in}} = 30$ MPa, $h_{\mathrm{in}} = 1$ nm, Fig. 7 plots the variations of the tensile modulus and yield strength with h_{GF} as given by Eqs. (11) and (12). It can be seen that thicker graphene flakes would result in a higher tensile stiffness ($E_{\mathrm{SGA}}^{\mathrm{t}}$), which is capped by the intrinsic modulus of the graphene flakes E_{GF}^{*}. In contrast, the tensile yield strength of SGA ($S_{\mathrm{SGA}}^{\mathrm{t}}$) decreases with h_{GF}.

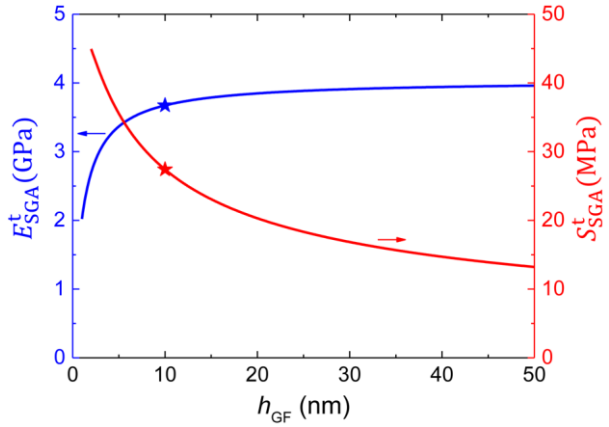

Fig. 7. The dependence of tensile modulus ($E_{\mathrm{SGA}}^{\mathrm{t}}$) and tensile yield strength ($S_{\mathrm{SGA}}^{\mathrm{t}}$) of SGA on the thickness (h_{GF}) of graphene flakes. Model parameters adopted in generating the curves: $E_{\mathrm{GF}} = 4$ GPa, $\nu_{\mathrm{GF}} = 0.1$, $G_{\mathrm{in}} = 400$ MPa, $\tau_{\mathrm{in}} = 30$ MPa, $h_{\mathrm{in}} = 1$ nm. The star symbols indicate the values of the SGA films we studied.

3.2 Compressive properties of SGA

As slender structures, the graphene flakes in an SGA film tend to buckle under critical compressive load (Bai et al., 2016; Ren et al., 2016; Wang et al., 2020). The post-buckling deformation of the graphene flakes under compressive load is recoverable and believed to

be the source of the elasticity as observed in experiments (Fig. 5(a)). Due to the mechanical constraint by the adjacent flakes along the out-of-plane direction, the post-buckling configuration of the discontinuous flakes was found similar to that of the continuous few-layer graphene sheets (Pan et al., 2019). Therefore, the structural discontinuity of the graphene flakes is neglected in our following discussion on the mechanical behavior of the SGA film under compressive load. The SGA film is idealized as a composite consisting of continuous few-layer graphene sheets and an artificial continuum matrix simulating the interfacial intermolecular interactions. To reveal the post-buckling stress-strain relation of the SGA film, we follow the approaches for modeling the composites with crimped reinforcements (Hsiao and Daniel, 1996a; Hsiao and Daniel, 1996b). The configuration of the buckled graphene sheets is assumed as a sinusoidal wave with period L and amplitude A, which can be formulated by expression $z(x) = A\left(1 - \cos\left(\frac{2\pi x}{L}\right)\right)$. The periodicity in waviness allows us to select a one-period-long representative volume element (RVE) for analysis, as shown in Fig. 8. As the period L and amplitude A of the graphene sheets may vary significantly under external load, this configuration should be deemed as the instant configuration, based on which the discussion on the mechanical response of the SGA to a compressive stress increment load ($\Delta\sigma_{xx}$) along the x direction will be made in the following.

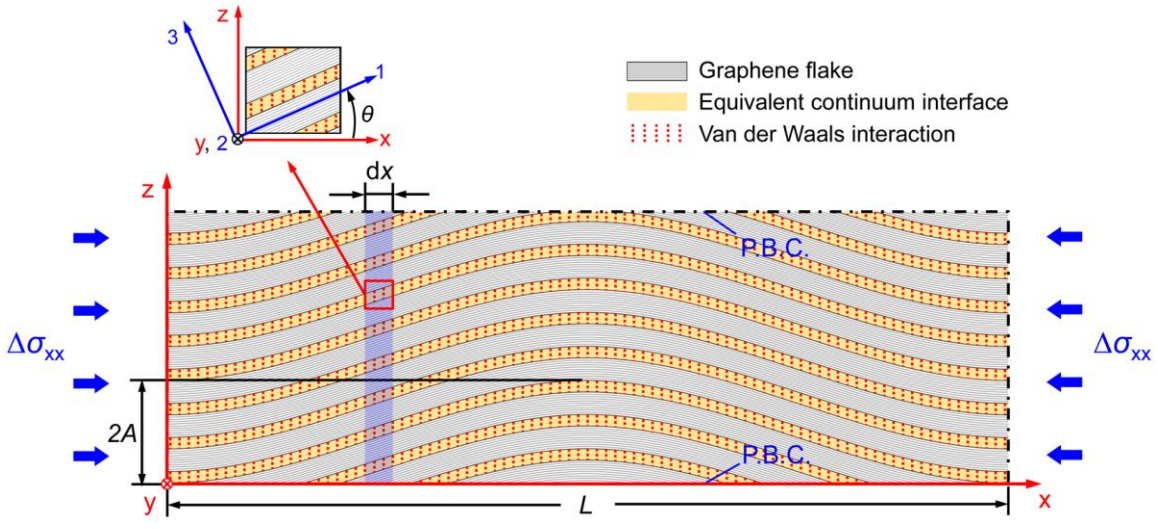

Fig. 8. Representative volume element of the composite model and coordinate systems adopted to model the mechanical behavior of the SGA under compression. P.B.C.: periodic boundary condition.

Firstly, we focus on an infinitesimally thin slice with thickness dx, which can be treated as a composite containing parallel graphene sheets at an oblique angle θ with respect to the x-axis embedded in the artificial matrix simulating the interfacial interaction, as shown in Fig. 8. With the assumption of periodic boundary condition along the z-direction and plane strain condition along the y-direction, the stress load $\Delta\sigma_{xx}$ along the x-direction would result in changes in the other two normal stress components $\Delta\sigma_{yy}(x)$ and $\Delta\sigma_{zz}(x)$ and one shear stress component $\Delta\tau_{xz}(x)$ but bring no change to the components τ_{yz} and τ_{xy}. The relationship between the incremental stress and incremental strain of the slice thus is given by

$$\begin{Bmatrix}\Delta\varepsilon_{xx}\\ \Delta\varepsilon_{yy}\\ \Delta\varepsilon_{zz}\\ \Delta\gamma_{yz}\\ \Delta\gamma_{xz}\\ \Delta\gamma_{xy}\end{Bmatrix} = [\bar{\boldsymbol{S}}]\begin{Bmatrix}\Delta\sigma_{xx}\\ \Delta\sigma_{yy}(x)\\ \Delta\sigma_{zz}(x)\\ 0\\ \Delta\tau_{xz}(x)\\ 0\end{Bmatrix} = \begin{Bmatrix}\bar{S}_{11}\Delta\sigma_{xx} + \bar{S}_{12}\Delta\sigma_{yy}(x) + \bar{S}_{13}\Delta\sigma_{zz}(x) + \bar{S}_{15}\Delta\tau_{xz}(x)\\ \bar{S}_{21}\Delta\sigma_{xx} + \bar{S}_{22}\Delta\sigma_{yy}(x) + \bar{S}_{23}\Delta\sigma_{zz}(x) + \bar{S}_{25}\Delta\tau_{xz}(x)\\ \bar{S}_{31}\Delta\sigma_{xx} + \bar{S}_{32}\Delta\sigma_{yy}(x) + \bar{S}_{33}\Delta\sigma_{zz}(x) + \bar{S}_{35}\Delta\tau_{xz}(x)\\ 0\\ \bar{S}_{51}\Delta\sigma_{xx} + \bar{S}_{52}\Delta\sigma_{yy}(x) + \bar{S}_{53}\Delta\sigma_{zz}(x) + \bar{S}_{55}\Delta\tau_{xz}(x)\\ 0\end{Bmatrix} \quad (13)$$

where $[\bar{\boldsymbol{S}}]$ is the instant compliance matrix of the slice in the fixed coordinate system x-y-z. Traditional composite theory indicates that (Hsiao and Daniel, 1996b).

$$[\bar{\boldsymbol{S}}] = [\boldsymbol{R}][\boldsymbol{T}]^{-1}[\boldsymbol{R}]^{-1}[\boldsymbol{S}][\boldsymbol{T}] \quad (14)$$

where $[\boldsymbol{S}]$ is the compliance matrix in the principal material coordinates 1-2-3, $[\boldsymbol{T}]$ the transformation matrix, $[\boldsymbol{R}]$ the Reuter matrix. Assuming the slice is transversely isotropic in the principal material coordinates 1-2-3, these matrices can be given by

$$[\boldsymbol{S}] = \begin{bmatrix} S_{11} & S_{12} & S_{13} & 0 & 0 & 0\\ S_{12} & S_{11} & S_{13} & 0 & 0 & 0\\ S_{13} & S_{13} & S_{33} & 0 & 0 & 0\\ 0 & 0 & 0 & S_{44} & 0 & 0\\ 0 & 0 & 0 & 0 & S_{44} & 0\\ 0 & 0 & 0 & 0 & 0 & 2(S_{11}-S_{12}) \end{bmatrix} \quad (15a)$$

$$[\boldsymbol{T}] = \begin{bmatrix} c^2 & 0 & s^2 & 0 & 2cs & 0\\ 0 & 1 & 0 & 0 & 0 & 0\\ s^2 & 0 & c^2 & 0 & -2cs & 0\\ 0 & 0 & 0 & c & 0 & -s\\ -cs & 0 & cs & 0 & c^2-s^2 & 0\\ 0 & 0 & 0 & s & 0 & c \end{bmatrix} \quad (15b)$$

$$[\boldsymbol{R}] = \begin{bmatrix} 1 & 0 & 0 & 0 & 0 & 0 \\ 0 & 1 & 0 & 0 & 0 & 0 \\ 0 & 0 & 1 & 0 & 0 & 0 \\ 0 & 0 & 0 & 2 & 0 & 0 \\ 0 & 0 & 0 & 0 & 2 & 0 \\ 0 & 0 & 0 & 0 & 0 & 2 \end{bmatrix} \tag{15c}$$

In Eq. (15a), the components $S_{11} = \frac{1}{E_{11}}$, $S_{33} = \frac{1}{E_{33}}$, $S_{12} = -\frac{\nu_{12}}{E_{11}}$, $S_{13} = -\frac{\nu_{13}}{E_{11}}$, $S_{44} = \frac{1}{G_{13}}$ with E_{11} and E_{33} being the in-plane and out-of-plane moduli (without buckling) of a planar SGA film respectively, and G_{13} the shear modulus in the 1-3 plane, and ν_{12} and ν_{13} the Poisson's ratio in the 1-2 and 1-3 planes, respectively. In Eq. (15b), $c = \cos\theta = \left[1 + \left(2\pi\rho\sin\left(\frac{2\pi x}{L}\right)\right)^2\right]^{-0.5}$, $s = \sin\theta = 2\pi\rho\sin\left(\frac{2\pi x}{L}\right)\left[1 + \left(2\pi\rho\sin\left(\frac{2\pi x}{L}\right)\right)^2\right]^{-0.5}$, with $\rho = A/L$ being the waviness ratio.

Plane strain condition along the *y*-direction implies $\Delta\varepsilon_{yy} \equiv 0$, which according to the second equation in Eq. (13) gives rise to

$$\Delta\tau_{xz}(x) = -\frac{\bar{S}_{21}}{\bar{S}_{25}}\Delta\sigma_{xx} - \frac{\bar{S}_{22}}{\bar{S}_{25}}\Delta\sigma_{yy}(x) - \frac{\bar{S}_{23}}{\bar{S}_{25}}\Delta\sigma_{zz}(x) \tag{16}$$

Since $\Delta\gamma_{xz} = \Delta(\tan\theta) = 2\pi\sin\left(\frac{2\pi x}{L}\right)\Delta\rho$, the fifth equation in Eq. (13) implies

$$\Delta\sigma_{yy}(x) = \frac{2\pi\sin\left(\frac{2\pi x}{L}\right)}{\bar{S}_{52}}\Delta\rho - \frac{\bar{S}_{51}}{\bar{S}_{52}}\Delta\sigma_{xx} - \frac{\bar{S}_{53}}{\bar{S}_{52}}\Delta\sigma_{zz}(x) - \frac{\bar{S}_{55}}{\bar{S}_{52}}\Delta\tau_{xz}(x) \tag{17}$$

Substituting Eq. (16) into Eq. (17) to eliminate $\Delta\tau_{xz}(x)$ yields

$$\Delta\sigma_{yy}(x) = \frac{2\pi\sin\left(\frac{2\pi x}{L}\right)\bar{S}_{25}}{\bar{S}_{52}\bar{S}_{25} - \bar{S}_{55}\bar{S}_{22}}\Delta\rho + \left(\frac{\bar{S}_{55}\bar{S}_{21} - \bar{S}_{51}\bar{S}_{25}}{\bar{S}_{52}\bar{S}_{25} - \bar{S}_{55}\bar{S}_{22}}\right)\Delta\sigma_{xx} + \left(\frac{\bar{S}_{55}\bar{S}_{23} - \bar{S}_{53}\bar{S}_{25}}{\bar{S}_{52}\bar{S}_{25} - \bar{S}_{55}\bar{S}_{22}}\right)\Delta\sigma_{zz}(x) \tag{18}$$

On the other hand, periodic boundary condition along the *z*-direction requires $\frac{\partial\Delta\varepsilon_{zz}}{\partial x} = 0$, implying that $\Delta\varepsilon_{zz}$ is a constant independent of x. Denoting $\Delta\varepsilon_{zz} = C$, according to the third equation in Eq. (13), we have

$$\Delta\varepsilon_{zz} = \bar{S}_{31}\Delta\sigma_{xx} + \bar{S}_{32}\Delta\sigma_{yy}(x) + \bar{S}_{33}\Delta\sigma_{zz}(x) + \bar{S}_{35}\Delta\tau_{xz}(x) = C \tag{19}$$

By substituting Eqs. (16) and (18) into Eq. (19) to eliminate $\Delta\tau_{xz}(x)$ and $\Delta\sigma_{yy}(x)$, $\Delta\sigma_{zz}$ can be given in terms of $\Delta\sigma_{xx}$ and $\Delta\rho$ as

$$\Delta\sigma_{zz}(x) = \frac{C}{g(x)} - \frac{f(x)}{g(x)}\,\Delta\sigma_{xx} - \frac{h(x)}{g(x)}\Delta\rho \tag{20}$$

where

$$f(x) = \frac{\bar{S}_{31}\bar{S}_{25}\bar{S}_{52} - \bar{S}_{35}\bar{S}_{21}\bar{S}_{52} - \bar{S}_{31}\bar{S}_{55}\bar{S}_{22} + \bar{S}_{32}\bar{S}_{55}\bar{S}_{21} - \bar{S}_{32}\bar{S}_{51}\bar{S}_{25} + \bar{S}_{35}\bar{S}_{22}\bar{S}_{51}}{\bar{S}_{52}\bar{S}_{25} - \bar{S}_{55}\bar{S}_{22}}$$

$$g(x) = \frac{\bar{S}_{33}\bar{S}_{52}\bar{S}_{25} - \bar{S}_{35}\bar{S}_{23}\bar{S}_{52} - \bar{S}_{33}\bar{S}_{55}\bar{S}_{22} + \bar{S}_{32}\bar{S}_{55}\bar{S}_{23} - \bar{S}_{32}\bar{S}_{53}\bar{S}_{25} + \bar{S}_{35}\bar{S}_{22}\bar{S}_{53}}{\bar{S}_{52}\bar{S}_{25} - \bar{S}_{55}\bar{S}_{22}}$$

$$h(x) = 2\pi\sin\left(\frac{2\pi x}{L}\right)\frac{\bar{S}_{32}\bar{S}_{25} - \bar{S}_{35}\bar{S}_{22}}{\bar{S}_{52}\bar{S}_{25} - \bar{S}_{55}\bar{S}_{22}}$$

Considering that the SGA along the *z*-direction is free of load, we propose an additional boundary condition as $\int_0^L \Delta\sigma_{zz}\,dx = 0$. Taking the integration on both sides of Eq. (20) and using this condition determine the constant *C* as

$$C = \frac{\Delta\sigma_{xx}\int_0^L \frac{f(x)}{g(x)}\mathrm{d}x + \Delta\rho\int_0^L \frac{h(x)}{g(x)}\mathrm{d}x}{\int_0^L \frac{1}{g(x)}\mathrm{d}x}$$

The first equation in Eq. (13) implies

$$\Delta\varepsilon_{xx} = \bar{S}_{11}\Delta\sigma_{xx} + \bar{S}_{12}\Delta\sigma_{yy}(x) + \bar{S}_{13}\Delta\sigma_{zz}(x) + \bar{S}_{15}\Delta\tau_{xz}(x) \tag{21}$$

Substituting Eqs. (16)(18)(20) into Eq. (21) to eliminate $\Delta\tau_{xz}(x)$, $\Delta\sigma_{yy}(x)$ and $\Delta\sigma_{zz}(x)$ yields

$$\Delta\varepsilon_{xx} = \left[p(x) - \frac{q(x)f(x)}{g(x)}\right]\Delta\sigma_{xx} + \left[r(x) - q(x)\frac{h(x)}{g(x)}\right]\Delta\rho + C\,\frac{q(x)}{g(x)} \tag{22}$$

where

$$p(x) = \frac{\bar{S}_{11}\bar{S}_{25}\bar{S}_{52} - \bar{S}_{15}\bar{S}_{21}\bar{S}_{52} - \bar{S}_{11}\bar{S}_{55}\bar{S}_{22} + \bar{S}_{12}\bar{S}_{55}\bar{S}_{21} - \bar{S}_{12}\bar{S}_{25}\bar{S}_{51} + \bar{S}_{15}\bar{S}_{22}\bar{S}_{51}}{(\bar{S}_{52}\bar{S}_{25} - \bar{S}_{55}\bar{S}_{22})}$$

$$q(x) = \frac{\bar{S}_{13}\bar{S}_{52}\bar{S}_{25} - \bar{S}_{15}\bar{S}_{23}\bar{S}_{52} - \bar{S}_{13}\bar{S}_{55}\bar{S}_{22} + \bar{S}_{12}\bar{S}_{55}\bar{S}_{23} - \bar{S}_{12}\bar{S}_{53}\bar{S}_{25} + \bar{S}_{15}\bar{S}_{22}\bar{S}_{53}}{(\bar{S}_{52}\bar{S}_{25} - \bar{S}_{55}\bar{S}_{22})}$$

$$r(x) = 2\pi\sin\left(\frac{2\pi x}{L}\right)\frac{(\bar{S}_{12}\bar{S}_{25} - \bar{S}_{15}\bar{S}_{22})}{(\bar{S}_{52}\bar{S}_{25} - \bar{S}_{55}\bar{S}_{22})}$$

Then the effective compressive strain of the RVE, which is equal to the averaged strain of a series of infinitesimal slices over one period along the *x*-direction, is given by

$$\Delta\varepsilon_{\mathrm{c}} = \frac{1}{L}\int_0^L \Delta\varepsilon_{xx}\mathrm{d}x = \Delta\sigma_{xx}M(\rho) + \Delta\rho N(\rho) \tag{23}$$

where

$$M(\rho) = \frac{1}{L}\left\{\frac{\int_0^L \frac{f(x)}{g(x)}dx \int_0^L \frac{q(x)}{g(x)}dx}{\int_0^L \frac{1}{g(x)}dx} + \int_0^L \left[\frac{p(x)g(x)-q(x)f(x)}{g(x)}\right]dx\right\}$$

$$N(\rho) = \frac{1}{L}\left\{\frac{\int_0^L \frac{h(x)}{g(x)}dx \int_0^L \frac{q(x)}{g(x)}dx}{\int_0^L \frac{1}{g(x)}dx} + \int_0^L \left[\frac{r(x)g(x)-q(x)h(x)}{g(x)}\right]dx\right\}$$

On the other hand, $\Delta\varepsilon_{\mathrm{c}}$ is geometrically correlated with $\Delta\rho$ through (see Appendix C)

$$\Delta\varepsilon_{\mathrm{c}} = \left[\frac{\mathbf{K}(k)/\mathbf{E}(k)}{\rho(1+4\pi^2\rho^2)} - \frac{1}{\rho}\right]\Delta\rho \tag{24}$$

where $\mathbf{K}(k) \equiv \int_0^{\frac{\pi}{2}} \frac{1}{\sqrt{1-k^2\sin^2\theta}}\mathrm{d}\theta$ and $\mathbf{E}(k) \equiv \int_0^{\frac{\pi}{2}} \sqrt{1-k^2\sin^2\theta}\,\mathrm{d}\theta$ are the complete elliptic integrals of the first and second kind respectively with $k \equiv \sqrt{\frac{4\pi^2\rho^2}{1+4\pi^2\rho^2}}$. Combining Eqs. (23) and (24) yields the tangent compressive modulus ($E^{\mathrm{c}}_{\mathrm{SGA}}$) of the SGA film as

$$E^{\mathrm{c}}_{\mathrm{SGA}}(\rho) \equiv \frac{\Delta\sigma_{xx}}{\Delta\varepsilon_{\mathrm{c}}} = \frac{\left[\frac{\mathbf{K}(k)/\mathbf{E}(k)}{\rho(1+4\pi^2\rho^2)}-\frac{1}{\rho}\right]-N(\rho)}{\left[\frac{\mathbf{K}(k)/\mathbf{E}(k)}{\rho(1+4\pi^2\rho^2)}-\frac{1}{\rho}\right]M(\rho)} \tag{25}$$

From Eq. (25), it can be seen that the compressive stiffness of SGA film ($E^{\mathrm{c}}_{\mathrm{SGA}}$) is a function of the waviness ratio ρ, whose initial value is given by

$$E^{\mathrm{c}}_{\mathrm{SGA}}(\rho \to 0) = \frac{2S_{12}(S_{12}-S_{13})S_{13}^2-2S_{11}^2S_{13}(S_{13}+S_{33})+2S_{11}^3S_{33}+2S_{11}(S_{13}^3-S_{12}^2S_{33}+S_{12}S_{13}S_{33})}{(S_{11}^2S_{13}^2+S_{12}^2S_{13}^2+S_{11}^3S_{33}-S_{11}S_{12}^2S_{33})S_{44}}. \tag{26}$$

If we assume $S_{13} = S_{12} = -\nu S_{11}$ (i.e., $\nu_{13} = \nu_{12} = \nu$), Eq. (26) can be further simplified to be

$$E^{\mathrm{c}}_{\mathrm{SGA}}(\rho \to 0) = \frac{2(\nu+1)S_{33}-2\nu^2(\nu+1)S_{11}}{[(\nu^2+1)\nu^2S_{11}+(1-\nu^2)S_{33}]S_{44}} \tag{27}$$

Considering that SGA is more condensed along the in-plane directions than in the out-of-plane direction, we may assume $S_{11} \ll S_{33}$. Eq. (27) can be further simplified to be

$E^c_{SGA}(\rho \to 0) \cong \frac{2(\nu+1)}{(1-\nu^2)} G_{13}$, showing that the initial compressive stiffness scales up with the shear stiffness (G_{13}).

When $\rho > 0$, the numerical calculation was applied to Eq. (25) to investigate the dependence of the compressive modulus (E^c_{SGA}) on the waviness ratio (ρ) as well as the affecting material parameters including E_{11}, E_{33}, G_{13}, ν_{12} and ν_{13}. Considering that the vertical stiffness (E_{33}) and Poisson's ratios (ν_{12} and ν_{13}) generally vary little, here we mainly focus on the effects of G_{13} and E_{11}.

Taking E_{11} as the tensile modulus of the SGA film, which is measured to be 3.5 GPa in the test above, Fig. 9(a) shows the dependence of E^c_{SGA} on G_{13} and ρ. It can be seen that if the shear stiffness G_{13} is taken in the range of 0.5-0.8 GPa, the compressive modulus E^c_{SGA} exhibits little variation as the waviness ratio ρ increases, just as we observed in the experiments (see Fig. 5(a)). In our SGA films, the graphene flakes adhere to each other through van der Waals forces only. By introducing other chemical bonding such as hydrogen bonding (Compton et al., 2012; Song et al., 2017), covalent bonding (Song et al., 2017), ionic bonding (Park et al., 2008) and polymetric intercalation (Chen et al., 2016; Wan et al., 2020) between the graphene flakes may lead to higher G_{13} and therefore produce SGA films with the higher compressive modulus (E^c_{SGA}) and higher elastic nonlinearity under compression, as predicated by Fig. 9(b). Based on the best fitting to our experimental results above, a reasonable estimation for our SGA films is $G_{13} = 0.7$ GPa, which is consistent with the value reported in literature (Soule and Nezbeda, 1968).

For given $G_{13} = 0.7$ GPa, Fig. 9(c) shows the dependence of E^c_{SGA} on E_{11} and ρ. It can be seen that E^c_{SGA} exhibits distinct evolutions with ρ, depending on the value of E_{11}. For higher E_{11}, E^c_{SGA} monotonically increases with ρ, while for lower E_{11} it monotonically decreases with ρ. E^c_{SGA} exhibits little variation with ρ when E_{11} falls in the range of 3-4.5 GPa (Fig. 9(c)). This may explain the excellent linearity of the compressive curves of SGA observed in our experiments. Moreover, Figs. 9 (c) and (d) show that higher E_{11} results in higher E^c_{SGA}. Therefore, application of thicker flakes, which would lead to higher tensile modulus (E^t_{SGA}) (see Fig. 7) and E_{11}, could produce SGA films with higher compressive modulus (E^c_{SGA}).

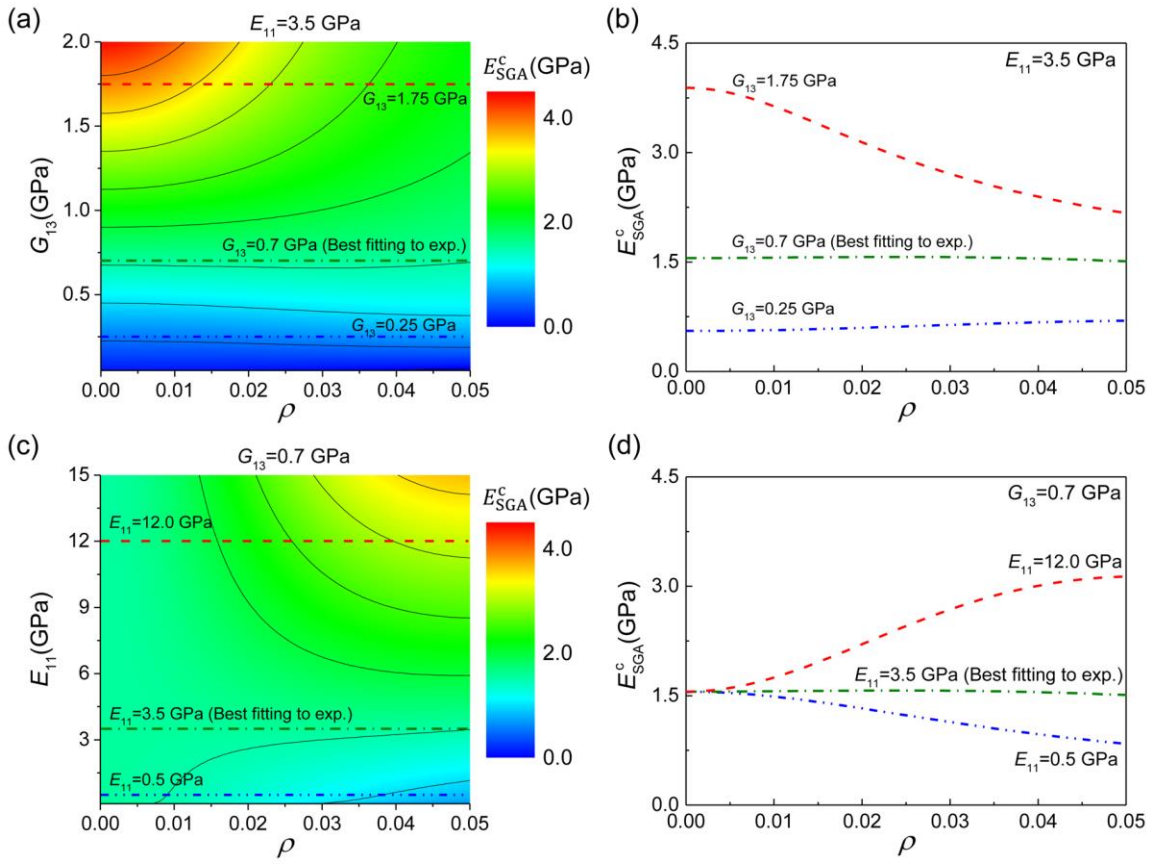

Fig. 9. Contours showing the dependence of the compressive modulus (E^c_{SGA}) of the SGA on (a, b) G_{13} for given $E_{11} = 3.5$ GPa, and (c, d) E_{11} for given $G_{13} = 0.7$ GPa. The rest model parameters adopted: $E_{33} = 100$ MPa, $\nu_{12} = \nu_{13}$ =0.1 (Wei and Yang, 2019).

4. Conclusion and discussion

In this paper, we experimentally investigated the mechanical behaviors of the SGA films under tensile and compressive loadings by taking advantage of the curling behavior of the SGA-based bilayers in response to temperature variation. It was shown that the SGA film exhibits elastic-perfectly plastic behavior under tension while purely elastic behavior under compression. This result verified our previous prediction based on the molecular dynamics simulations (Wang et al., 2020). Theoretical modeling was further carried out to reveal the structural basis accounting for such asymmetric elastoplasticity. Three feature parameters characterizing the mechanical behaviors of the SGA, including tensile modulus (E^t_{SGA}), tensile yield strength (S^t_{SGA}), and compressive modulus (E^c_{SGA}), are formulated as the functions of the structural dimensions as well as the mechanical properties of the building flakes and the inter-flake interface, showing quantitatively the structure-property

relations of the SGA. Our work not only provides a facile yet feasible method to measure the mechanical behaviors of the stacked assemblies of 2D materials, but also sheds lights on the structural dependence of their properties, which would allow us to controllably manipulate the mechanical properties of the stacked assemblies of 2D materials by tuning the size and thickness of the building flakes or regulating the interfacial bonding between flakes. This will be of great practical value to the application of the SGA and other alike stacked assemblies of 2D materials in sensors and actuators (He et al., 2019; Wang et al., 2020). Nevertheless, limitations remain present in our work. For example, when modeling the tensile behavior of the SGA, all the graphene flakes were assumed identical and organized regularly in a staggered structure. In reality, however, the shape, size, and thickness of the graphene flakes might differ widely (Yang et al., 2019; Yang et al., 2018; Yang and Yao, 2020) and some flakes may be stacked in a tilted way, resulting in voids and flaws in the SGA. Additionally, initial wrinkles, ripples or corrugations often exist in soft membranes like graphene flakes (Chang et al., 2019; Liu et al., 2011b). These structural imperfection would largely affect the mechanical properties of the stacking structure (Xie and Wei, 2021). For example, the existence of initial wrinkles or curvatures of the graphene flakes would lead to lower tensile modulus of the SGA film especially at small strain before being flattened. Moreover, when preparing the SGA samples using the L-B method (He et al., 2019), the graphene flakes were assembled and condensed by the change of water surface tension induced by the submersion of a piece of sponge. The extent of condensation, which cannot be controlled precisely, may affect the structure of the obtained SGA. The effects of these issues on the mechanical behaviors of SGA are beyond the scope of this paper and will be addressed in our future work.

Appendix A. Measurement of the coefficient of thermal expansion of PE

Firstly, a graphene-ethanol solution is sprayed onto the surface of a PE film sample, resulting in random speckles after drying. Then, the PE film is hanged in a temperature test chamber, where the temperature varies (increases or decreases) from the room temperature (25℃) at a rate of 0.5℃/min. Every 4 minutes, a digital photo is taken on the speckled PE surface to capture the thermally-induced deformation of the film. Based on these photos,

the strains of PE film along the longitudinal and transverse directions at different temperatures are calculated via image processing (ImageJ). Linear curve-fitting on the data, as shown in Fig. A1, gives the coefficients of thermal expansion along the longitudinal and transverse directions as $3.58 \times 10^{-4}/℃$ and $2.54 \times 10^{-4}/℃$, respectively.

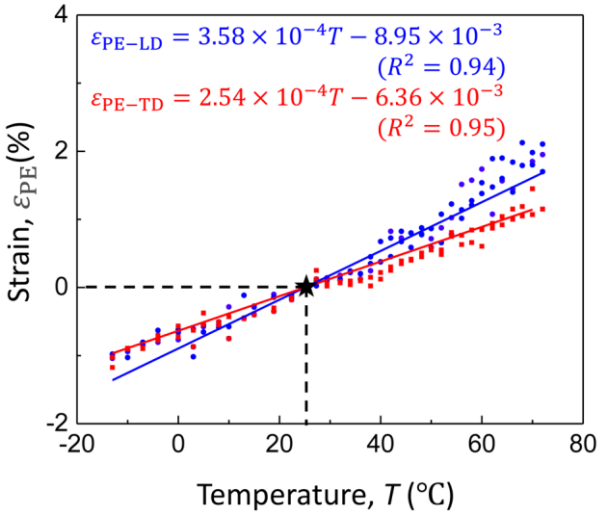

Fig. A1. The deformation (in terms of strain, ε_{PE}) of a PE film along the longitudinal (LD) and transverse directions (TD) with the temperature.

Appendix B. Measurement of the elastic modulus of PE

Tensile tests are carried out on PE film samples with a dynamic mechanical analyzer (DMA 8000, PerkinElmer) at different temperatures ranging from $-15℃$ to $65℃$, which well covers the temperature range employed in the stress-strain curve measurement. The measured elastic modulus of PE (E_{PE}), as shown in Fig. B1, exhibits a strong temperature dependence, which can be perfectly described by a quadratic fitting curve $E_{PE}(T) = 0.045T^2 - 6.53T + 284.6$. This temperature-dependent elastic modulus of PE will be applied when determining the stress-strain curve of SGA film.

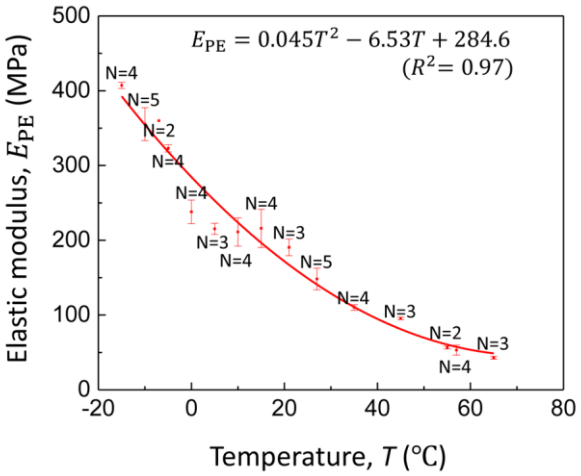

Fig. B1. Dependence of the elastic modulus of PE film (E_{PE}) on temperature (T). Here N stands for the number of the tested samples.

Appendix C. A geometrical correlation between $\Delta\varepsilon_c$ and $\Delta\rho$

For a wavy graphene layer with sinusoidal profile given by $z(x) = A\left(1 - \cos\left(\frac{2\pi x}{L}\right)\right)$, its overall length in a period is

$$s = 4\int_0^{L/4}\sqrt{1+z'(x)^2}\,dx = 4\int_0^{L/4}\sqrt{1+\frac{4\pi^2 A^2}{L^2}\sin^2\left(2\pi\frac{x}{L}\right)}\,\mathrm{d}x \tag{C1}$$

Letting $u = 2\pi\frac{(x-L/4)}{L}$ and $\rho = A/L$, Eq. (C1) can be simplified to be

$$s = \frac{2L\sqrt{1+4\pi^2\rho^2}}{\pi}\int_0^{\frac{\pi}{2}}\sqrt{1-\frac{4\pi^2\rho^2}{1+4\pi^2\rho^2}\sin^2(u)}\,\mathrm{d}u = \frac{2L\sqrt{1+4\pi^2\rho^2}}{\pi}\cdot\mathbf{E}(k), \tag{C2}$$

where $\mathbf{E}(k) \equiv \int_0^{\frac{\pi}{2}}\sqrt{1-k^2\sin^2\theta}\,\mathrm{d}\theta$ is the complete elliptic integral of the second kind with $k \equiv \sqrt{\frac{4\pi^2\rho^2}{1+4\pi^2\rho^2}}$. We assume that the overall length of the graphene layer is unchanged during the deformation under compression. Then we have

$$\frac{\mathrm{d}s}{\mathrm{d}\rho} = \frac{2\sqrt{1+4\pi^2\rho^2}}{\pi}\mathbf{E}(k)\frac{\mathrm{d}L}{\mathrm{d}\rho} + \frac{8L\pi^2\rho}{\pi\sqrt{1+4\pi^2\rho^2}}\mathbf{E}(k) + \frac{2L\sqrt{1+4\pi^2\rho^2}}{\pi}\mathbf{E}'(k)\frac{\mathrm{d}k}{\mathrm{d}\rho} = 0 \tag{C3}$$

where $\mathbf{E}'(k) = \frac{\mathrm{d}\mathbf{E}(k)}{\mathrm{d}k} = \frac{\mathbf{E}(k)-\mathbf{K}(k)}{k}$ with $\mathbf{K}(k) = \int_0^{\frac{\pi}{2}} \frac{1}{\sqrt{1-k^2\sin^2\theta}}\mathrm{d}\theta$ being the complete elliptic integral of the first kind. Substituting this relationship back to Eq. (C3) to eliminate $\mathbf{E}'(k)$, we have

$$\frac{\mathrm{d}L}{L\mathrm{d}\rho} = \frac{\mathbf{K}(k)/\mathbf{E}(k)}{\rho(1+4\pi^2\rho^2)} - \frac{1}{\rho} \tag{C4}$$

If we do not distinguish the engineering and true strains at small strain, $\mathrm{d}\varepsilon_\mathrm{c} = \frac{\mathrm{d}L}{L}$. Eq. (C4) then can be rewritten as

$$\frac{\mathrm{d}\varepsilon_\mathrm{c}}{\mathrm{d}\rho} = \frac{\mathbf{K}(k)/\mathbf{E}(k)}{\rho(1+4\pi^2\rho^2)} - \frac{1}{\rho} \tag{C5}$$

This gives rise to the correlation between $\Delta\varepsilon_\mathrm{c}$ and $\Delta\rho$ as

$$\Delta\varepsilon_\mathrm{c} = \left[\frac{\mathbf{K}(k)/\mathbf{E}(k)}{\rho(1+4\pi^2\rho^2)} - \frac{1}{\rho}\right]\Delta\rho \tag{C6}$$

Acknowledgment

Support for this work from the National Natural Science Foundation of China (Grant no. 11772283) is acknowledged.

References

Bai, Z., Su, Y., Ji, B., 2016. Buckling behaviors of staggered nanostructure of biological materials. Journal of Applied Mechanics 83, 031011.

Bhimanapati, G.R., Lin, Z., Meunier, V., Jung, Y., Cha, J., Das, S., Xiao, D., Son, Y., Strano, M.S., Cooper, V.R., 2015. Recent advances in two-dimensional materials beyond graphene. ACS Nano 9, 11509-11539.

Chang, Z., Yang, R., Wei, Y., 2019. The linear-dependence of adhesion strength and adhesion range on temperature in soft membranes. Journal of the Mechanics and Physics of Solids 132, 103697.

Chen, K., Tang, X., Yue, Y., Zhao, H., Guo, L., 2016. Strong and tough layered nanocomposites with buried interfaces. ACS Nano 10, 4816-4827.

Chen, W., Yan, L., Bangal, P.R., 2010. Preparation of graphene by the rapid and mild thermal reduction of graphene oxide induced by microwaves. Carbon 48, 1146-1152.

563 Coleman, J.N., Lotya, M., O'Neill, A., Bergin, S.D., King, P.J., Khan, U., Young, K., Gaucher, A.,
564 De, S., Smith, R.J., 2011. Two-dimensional nanosheets produced by liquid exfoliation of layered
565 materials. Science 331, 568-571.

566 Compton, O.C., Cranford, S.W., Putz, K.W., An, Z., Brinson, L.C., Buehler, M.J., Nguyen, S.T.,
567 2012. Tuning the mechanical properties of graphene oxide paper and its associated polymer
568 nanocomposites by controlling cooperative intersheet hydrogen bonding. ACS Nano 6, 2008-2019.

569 Fiori, G., Bonaccorso, F., Iannaccone, G., Palacios, T., Neumaier, D., Seabaugh, A., Banerjee, S.K.,
570 Colombo, L., 2014. Electronics based on two-dimensional materials. Nature Nanotechnology 9,
571 768-779.

572 Freund, L.B., Suresh, S., 2004. Thin film materials: stress, defect formation and surface evolution.
573 Cambridge university press, Cambridge, UK.

574 Gao, H., Ji, B., Jäger, I.L., Arzt, E., Fratzl, P., 2003. Materials become insensitive to flaws at
575 nanoscale: lessons from nature. Proceedings of the National Academy of Sciences of the United
576 States of America 100, 5597-5600.

577 Geim, A.K., 2009. Graphene: status and prospects. Science 324, 1530-1534.

578 Gupta, A., Sakthivel, T., Seal, S., 2015. Recent development in 2D materials beyond graphene.
579 Progress in Materials Science 73, 44-126.

580 Hanlon, D., Backes, C., Doherty, E., Cucinotta, C.S., Berner, N.C., Boland, C., Lee, K., Harvey,
581 A., Lynch, P., Gholamvand, Z., 2015. Liquid exfoliation of solvent-stabilized few-layer black
582 phosphorus for applications beyond electronics. Nature Communications 6, 1-11.

583 He, J., Xiao, P., Lu, W., Shi, J., Zhang, L., Liang, Y., Pan, C., Kuo, S.-W., Chen, T., 2019. A
584 Universal high accuracy wearable pulse monitoring system via high sensitivity and large linearity
585 graphene pressure sensor. Nano Energy 59, 422-433.

586 Hernandez, Y., Nicolosi, V., Lotya, M., Blighe, F.M., Sun, Z., De, S., McGovern, I., Holland, B.,
587 Byrne, M., Gun'Ko, Y.K., Boland, J.J., Niraj, P., Duesberg, G., Krishnamurthy, S., Goodhue, R.,
588 Hutchison, J., Scardaci, V., Ferrari, A.C., Coleman, J.N., 2008. High-yield production of graphene
589 by liquid-phase exfoliation of graphite. Nature Nanotechnology 3, 563-568.

590 Hsiao, H., Daniel, I., 1996a. Effect of fiber waviness on stiffness and strength reduction of
591 unidirectional composites under compressive loading. Composites Science and Technology 56,
592 581-593.

593 Hsiao, H., Daniel, I., 1996b. Elastic properties of composites with fiber waviness. Composites Part
594 A: Applied Science and Manufacturing 27, 931-941.

595 Huang, Y., Sutter, E., Shi, N.N., Zheng, J., Yang, T., Englund, D., Gao, H.-J., Sutter, P., 2015.
596 Reliable exfoliation of large-area high-quality flakes of graphene and other two-dimensional
597 materials. ACS Nano 9, 10612-10620.

598 Huo, N., Konstantatos, G., 2018. Recent progress and future prospects of 2D-based photodetectors.
599 Advanced Materials 30, 1801164.

Jeon, J., Jang, S.K., Jeon, S.M., Yoo, G., Jang, Y.H., Park, J.-H., Lee, S., 2015. Layer-controlled CVD growth of large-area two-dimensional MoS_2 films. Nanoscale 7, 1688-1695.

Kim, H., Abdala, A.A., Macosko, C., 2010. Graphene/polymer nanocomposites. Macromolecules 43, 6515-6530.

Kim, S.J., Choi, K., Lee, B., Kim, Y., Hong, B.H., 2015. Materials for flexible, stretchable electronics: graphene and 2D materials. Annual Review of Materials Research 45, 63-84.

Ladizesky, N., Ward, I., 1971. Determination of Poisson's ratio and Young's modulus of low-density polyethylene. Journal of Macromolecular Science, Part B: Physics 5, 661-692.

Li, P., Cao, K., Jiang, C., Xu, S., Gao, L., Xiao, X., Lu, Y., 2019. In situ tensile fracturing of multilayer graphene nanosheets for their in-plane mechanical properties. Nanotechnology 30, 475708.

Li, Z., Yang, Q.-S., 2020. Sensing mechanism of flexible and stretchable composites based on stacked graphene. Materials & Design 187, 108384.

Liu, G., Ji, B., Hwang, K.-C., Khoo, B.C., 2011a. Analytical solutions of the displacement and stress fields of the nanocomposite structure of biological materials. Composites Science and Technology 71, 1190-1195.

Liu, N., Pan, Z., Fu, L., Zhang, C., Dai, B., Liu, Z., 2011b. The origin of wrinkles on transferred graphene. Nano Research 4, 996.

Long, M., Wang, P., Fang, H., Hu, W., 2019. Progress, challenges, and opportunities for 2D material based photodetectors. Advanced Functional Materials 29, 1803807.

Nakada, K., Fujita, M., Dresselhaus, G., Dresselhaus, M.S., 1996. Edge state in graphene ribbons: Nanometer size effect and edge shape dependence. Physical Review B 54, 17954.

Novoselov, K.S., Geim, A.K., Morozov, S.V., Jiang, D., Zhang, Y., Dubonos, S.V., Grigorieva, I.V., Firsov, A.A., 2004. Electric field effect in atomically thin carbon films. Science 306, 666-669.

Pan, F., Wang, G., Liu, L., Chen, Y., Zhang, Z., Shi, X., 2019. Bending induced interlayer shearing, rippling and kink buckling of multilayered graphene sheets. Journal of the Mechanics and Physics of Solids 122, 340-363.

Pang, Y., Yang, J., Curtis, T.E., Luo, S., Huang, D., Feng, Z., Morales-Ferreiro, J.O., Sapkota, P., Lei, F., Zhang, J., 2019. Exfoliated graphene leads to exceptional mechanical properties of polymer composite films. ACS Nano 13, 1097-1106.

Park, S., Lee, K.-S., Bozoklu, G., Cai, W., Nguyen, S.T., Ruoff, R.S., 2008. Graphene oxide papers modified by divalent ions—enhancing mechanical properties via chemical cross-linking. ACS Nano 2, 572-578.

Pomerantseva, E., Gogotsi, Y., 2017. Two-dimensional heterostructures for energy storage. Nature Energy 2, 1-6.

635 Potts, J.R., Dreyer, D.R., Bielawski, C.W., Ruoff, R.S., 2011. Graphene-based polymer
636 nanocomposites. Polymer 52, 5-25.

637 Ren, M., Liu, Y., Liu, J.Z., Wang, L., Zheng, Q., 2016. Anomalous elastic buckling of layered
638 crystalline materials in the absence of structure slenderness. Journal of the Mechanics and Physics
639 of Solids 88, 83-99.

640 Song, P., Xu, Z., Wu, Y., Cheng, Q., Guo, Q., Wang, H., 2017. Super-tough artificial nacre based
641 on graphene oxide via synergistic interface interactions of π-π stacking and hydrogen bonding.
642 Carbon 111, 807-812.

643 Sorkin, V., Cai, Y., Ong, Z., Zhang, G., Zhang, Y.-W., 2017. Recent advances in the study of
644 phosphorene and its nanostructures. Critical Reviews in Solid State and Materials Sciences 42, 1-
645 82.

646 Soule, D., Nezbeda, C., 1968. Direct basal - plane shear in single - crystal graphite. Journal of
647 Applied Physics 39, 5122-5139.

648 Wan, S., Li, X., Wang, Y., Chen, Y., Xie, X., Yang, R., Tomsia, A.P., Jiang, L., Cheng, Q., 2020.
649 Strong sequentially bridged MXene sheets. Proceedings of the National Academy of Sciences of
650 the United States of America 117, 27154-27161.

651 Wang, S., Gao, Y., Wei, A., Xiao, P., Liang, Y., Lu, W., Chen, C., Zhang, C., Yang, G., Yao, H.,
652 2020. Asymmetric elastoplasticity of stacked graphene assembly actualizes programmable
653 untethered soft robotics. Nature Communications 11, 1-12.

654 Wei, Y., Yang, R., 2019. Nanomechanics of graphene. National Science Review 6, 324-348.

655 Xie, W., Wei, Y., 2021. Roughening for Strengthening and Toughening in Monolayer Carbon
656 Based Composites. Nano Letters 21, 4823–4829.

657 Yang, J., Shen, X., Wang, C., Chai, Y., Yao, H., 2019. Deciphering mechanical properties of 2D
658 materials from the size distribution of exfoliated fragments. Extreme Mechanics Letters 29, 100473.

659 Yang, J., Wang, Y., Li, Y., Gao, H., Chai, Y., Yao, H., 2018. Edge orientations of mechanically
660 exfoliated anisotropic two-dimensional materials. Journal of the Mechanics and Physics of Solids
661 112, 157-168.

662 Yang, J., Yao, H., 2020. Automated identification and characterization of two-dimensional
663 materials via machine learning-based processing of optical microscope images. Extreme
664 Mechanics Letters 39, 100771.

665 Yao, H., Song, Z., Xu, Z., Gao, H., 2013. Cracks fail to intensify stress in nacreous composites.
666 Composites Science and Technology 81, 24-29.

667 Zhang, X., Hou, L., Ciesielski, A., Samorì, P., 2016. 2D materials beyond graphene for high-
668 performance energy storage applications. Advanced Energy Materials 6, 1600671.

669